J Mater Sci (2011) 46:6518–6527
DOI 10.1007/s10853-011-5598-1

Texture evolution in an Al–Cu alloy during equal channel angular pressing: the effect of starting microstructure

P. Venkatachalam · Shibayan Roy · B. Ravisankar · V. Thomas Paul · M. Vijayalakshmi · Satyam Suwas

Received: 20 December 2010 / Accepted: 28 April 2011 / Published online: 17 May 2011

Abstract In this article, the effect of initial microstructure on the texture evolution in 2014 Al alloy during equal channel angular pressing (ECAP) through route A has been reported. Three heat treatment conditions were chosen to generate the initial microstructures, namely (i) the recrystallization anneal (as-received), (ii) solution treatment at 768 K for 1 h, and (iii) solution treatment (768 K for 1 h) plus aging at 468 K for 5 h. Texture analyses were performed using orientation distribution function (ODF) method. The texture strength after ECAP processing was different for the three samples in the order, solutionised > solutionised plus aged condition > as-received. The prominent texture components were $A_E/\bar{A}_E$ and $B_E/\bar{B}_E$ in addition to several weaker components for the three materials. The strong texture evolution in solutionised condition has been attributed to higher strain hardening of the matrix due to higher amount of solute. In case of the as-received as well as solutionised plus aged alloy, the weaker texture could be due to the strain scattering from extensive precipitate fragmentation and dissolution during ECAP.

P. Venkatachalam (✉) · B. Ravisankar
Department of Metallurgical and Materials Engineering, National Institute of Technology, Tiruchirappalli 620015, India
e-mail: premvenkat76@gmail.com

S. Roy · S. Suwas
Department of Materials Engineering, Indian Institute of Science, Bangalore 560012, India

V. T. Paul · M. Vijayalakshmi
Physical Metallurgy Division, Indira Gandhi Centre for Atomic Research, Kalpakkam 603102, India

Introduction

The ECAP is one of the most common severe plastic deformation methods for producing ultra-fine microstructures in metals, alloys, and composites [1–5]. In addition to the significant effect on mechanical properties, ECAP is also associated with the development of specific crystallographic texture [6–9]. Texture evolution in material after ECAP is a strong function of processing route as well as the initial material variable, e.g., initial composition and texture [10–13]. These studies mainly deal with the texture formation in pure face centered cubic (fcc) metals like Al, Cu, and a few in their alloys [14–20]. It is, however, important to know the role of initial microstructure on the final texture formation after ECAP.

Aluminum alloys are known to be an important class of structural materials. While a large number of articles are published on the evolution of texture and microstructure during ECAP of non-heat treatable alloys [21–24], only a few are available on the heat treatable alloys. In this study, an attempt has been made to characterize the texture evolution in a heat treatable Al alloy 2014 during ECAP. These alloys are generally available in the form of heat treated and naturally aged condition, solution treated condition, and solution treated plus aged condition. In this study, all the three microstructural conditions have been subjected to ECAP to examine texture formation in the presence of fine precipitates (as-received), a relatively coarser precipitate (solution treated and aged) and in the absence of any precipitate (solution treated).

The effect of ECAP on microstructural evolution and mechanical properties of the three types of starting materials has been previously reported by the authors in [25]. However, it is well known that the crystallographic texture is an inseparable component of microstructure. Therefore,

a research program has been formulated to examine texture evolution during ECAP processing of these materials having large differences in the microstructures. A rigorous analysis of the experimental textures has been carried out using pole figures and ODFs to understand the texture evolution at individual conditions. Finally, the texture evolution at each condition has been interpreted as a function of the corresponding microstructural features.

Experimental procedures

Material and processing

The starting material used for this study was commercially available 2014 Al alloy in the form of an extruded rod with 13 mm diameter. The chemical composition of the starting material is given in Table 1. As mentioned earlier, different microstructural conditions of the alloy 2014 have been subjected to ECAP, namely, (i) the as-received material with fine precipitates due to natural aging, (ii) the material solution treated and quenched, and (iii) the material solution treated and aged. The solution treatment was carried out at 768 K for 1 h followed by quenching to room temperature (hereafter referred to as ST), while the aging treatment was done at 468 K for 5 h (hereafter referred to as ST + A). The appropriate aging condition was optimized on the basis of experimentally measured hardness values as a function of aging time (see Fig. 1). The maximum hardness was observed after 5 h of aging so that the aging time was fixed for 5 h.

The as-received material, the material after solution treatment, and the material obtained after solution treatment followed by aging was considered for further ECAP experiments. The samples corresponding to these three conditions were machined to fit in an ECAP die with circular cross section having 12 mm diameter of the channels. The inter-channel angle of the die was $\Phi = 90°$ and the outer arc of curvature was $\Psi = 20°$. The schematics of the die are shown in Fig. 2. The ECAP experiments were carried out using a hydraulic press at a crosshead speed of 0.5 mm/s at room temperature up to five passes for all three starting conditions. The equivalent strain per pass for the employed design was 1.07 so that the total imposed strain after five pass becomes 5.35 [26]. The samples were processed following the route A i.e., no rotations was applied between subsequent passes. They were well lubricated using MoS_2 between successive ECAP passes.

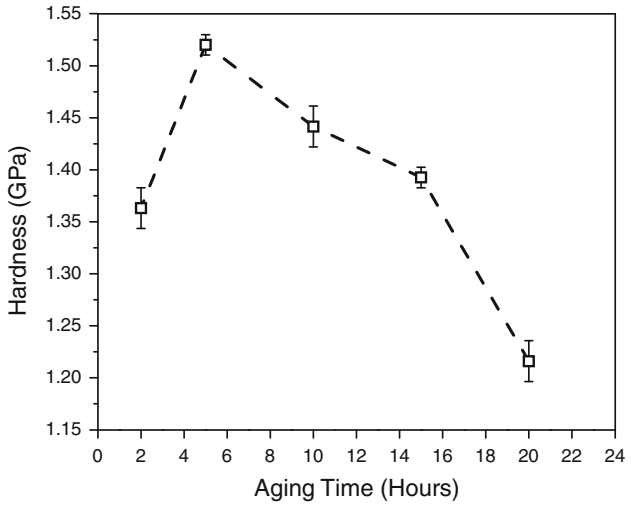

Fig. 1 The aging curve obtained for the as-received alloy after solution treatment showing the hardness values as a function of the aging time

The primary objective of this study is to understand the role of starting microstructure on the final microstructure and texture evolution in case of an Al–Cu alloy. Ideally speaking, the effect of deformation on the microstructural changes (e.g., grain refinement) as well as texture evolution saturates only after the first few passes during any SPD processes, as has been clearly identified by various researchers [1]. Similar trend has been observed in this investigation wherein the microstructure and texture do not largely vary after four passes. An indirect indication of microstructural consistency can be obtained from the hardness invariance with respect to the number of ECAE cycles after 4th cycle as shown in Fig. 6. In that perspective, the ECAE processing is carried out only up to five cycles in this study.

Microstructural examination

The microstructures of deformed materials were examined under transmission electron microscope (TEM) using Philips-TEM operated at an accelerating voltage of 200 kV. The thin foil TEM specimens were prepared from the middle of the specimens (see Fig. 3) by mechanical polishing followed by twin jet electro polishing using a solution of 10% perchloric acid + 90% methanol at the temperature −20 °C.

Table 1 Chemical composition of the as-received 2014 Al alloy (wt%)

Si	Fe	Cu	Mn	Mg	Cr	Ni	Zn	Ca	Al
0.776	0.234	4.32	0.831	0.751	0.0084	0.012	0.0946	0.0071	Balance

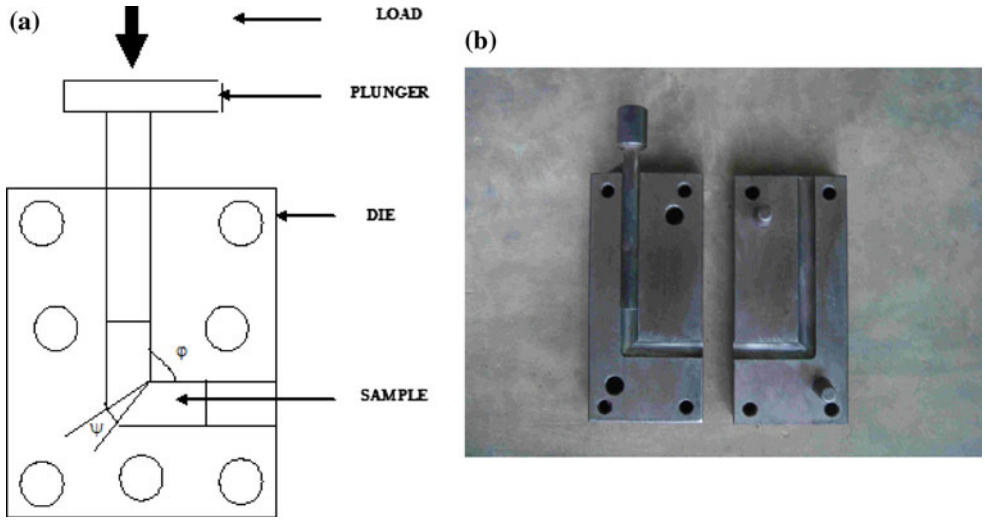

Fig. 2 **a** Schematic and **b** photograph of ECAP die employed in this study

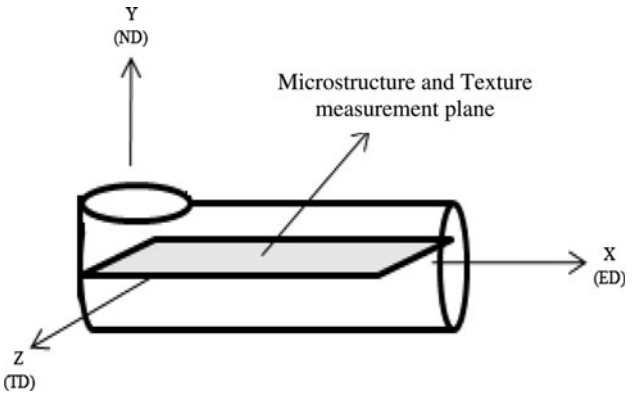

Fig. 3 Schematic showing the geometry of the ECAP processed sample along with the measurement plane for microstructure and texture characterization

The microstructural sizes were calculated from several TEM images (not less than 20 in each case) to obtain a global statistical reliability. The calculation was based on the linear intercept method using commercially available image analysis software (Sigma Scan Pro®, Systat Software, Inc., USA). The measurement was carried out by drawing numerous horizontal and vertical test lines at almost equivalent distances to obtain statistically averaged intercept values of not less than 99% confidence level. Edge grains were also included in the measurement scheme. From the measured values, a cumulative distribution (in terms of number fractions) of intercept length was obtained. Finally, the weighted average along with the corresponding error value was calculated from the distribution. A proportionality constant of 1.56 was used to convert the average linear intercept lengths into the corresponding spatial sizes according to the *ASTM standard number E112-96.*

X-ray characterization

The X-ray diffraction pattern of the ECAP-processed samples was recorded on the electro-polished surface by using X'PertPro®, PANalytical in CuK_α radiation. The diffraction patterns were recorded by varying 2θ from 30° to 120° in a continuous scan mode. The data were recorded in a 2θ interval of 0.017°. The time for collecting the data per step was 200 s. The diffraction patterns were corrected for the instrumental broadening using a silicon sample, which had large crystallites and was free from the defects.

Texture measurement

The texture measurements were performed on the mid-horizontal plane (TD-ED plane) of the samples, before and after the ECAP parallel to the ECAP direction (see Fig. 3). A Bruker D8 texture goniometer having Schultz reflection geometry and with CuK_α ($\lambda = 1.5406$ Å) radiation was employed for this. Four incomplete pole figures viz. (111), (200), (220), and (113) were recorded for each of the samples. The ODFs were calculated from the experimentally obtained pole figures in Labotex® software using ADC algorithm [27]. The ODF calculation was carried out without any rotation or symmetrization of the experimental data. The initial ODF was rotated afterward with respect to φ_1 and φ axes in such a way that the recalculated pole figures were finally represented in correct frame of reference where the ideal shear texture for ECAP processing are clearly visible. This measurement scheme was chosen to ensure the ideal conditions of texture development. It has been strongly reported by various researchers that the strain distribution and the resultant ECAP texture evolution is inherently heterogeneous in the ND–TD plane [7]. In order to avoid this experimental difficulty, the presently applied

texture measurement scheme is generally accepted and reported previously by various researchers [10–14]. Finally, the recalculated pole figures and appropriate ODF sections were plotted on the TD plane without imposing any sample symmetry.

Results and discussions

Microstructure evolution

Figure 4 shows the microstructures of the as-received, solution-treated, and solution treated plus aged materials before the ECAP processing. The as-received material consists of fully recrystallized grains with fine precipitates of size ~90 nm distributed all over the Al matrix (see Fig. 4a). These precipitates formed due to the natural aging. The recrystallized grains were almost equiaxed with an average size of ~2–3 μm. Figure 4b shows the microstructure of the alloy in the solution-treated condition. The microstructure consists of recrystallized grains without any precipitates inside them. The grain size at this condition was measured to be ~3–4 μm. After the solution treatment and aging, precipitates of size ~125 nm reappeared in the Al matrix (see Fig. 4c). It is to be noted that the precipitates in this condition were much coarser than those present in the matrix of the as-received material. The selected area diffraction pattern as well as EDS spectrum obtained from the precipitate phase present in the ST + A starting material confirms that they were of $CuAl_2$ type (see Fig. 4d, e).

Figure 5 shows the TEM bright-field micrographs from the three materials after the ECAP processing up to five

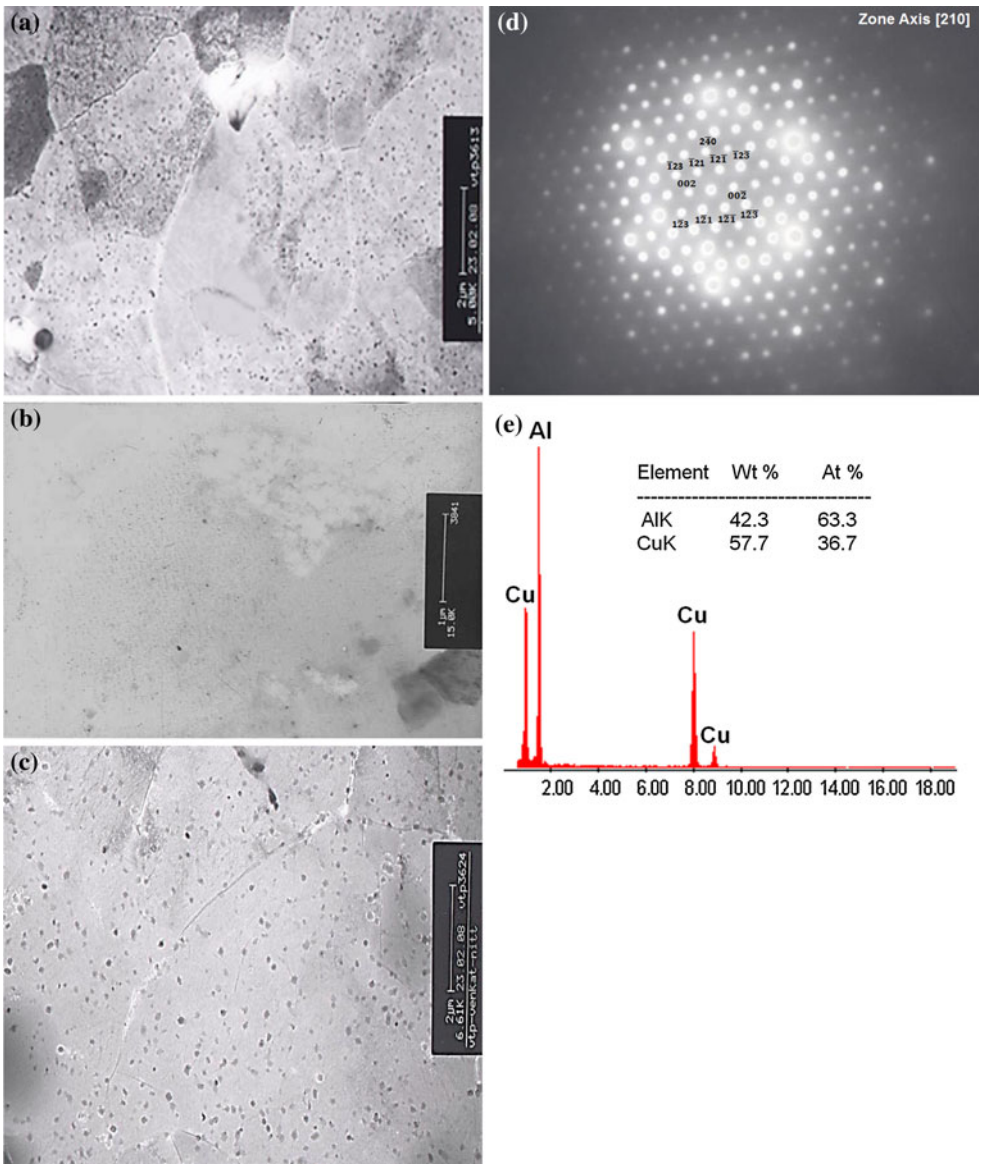

Fig. 4 Bright field TEM micrographs showing the microstructures of starting materials before ECAP in **a** as-received condition, **b** after solution treatment, and **c** at solutionised + aged condition. **d** and **e** shows the selected area diffraction pattern and EDS spectrum obtained from the precipitate phase in **c**, respectively

passes. As evident from these microstructures, the grains are sheared during ECAP processing along the shear direction (a direction 45° from the ECAP direction) leading to elongated grain structures in all the three materials. In case of the ECAP-processed as-received material, grains were sheared along the shear axis with the long grain axis being inclined in the direction of shear axis. For this material, the grain size was 280 ± 10 nm after five passes of ECAP, as measured from the TEM micrographs. The fine precipitates that were present in the as-received material were completely dissolved in the matrix (see Fig. 5a). The microstructural features for the ST material after ECAP processing displays completely deformed grains, which were slightly elongated along the shear direction. The grain size at this condition was 270 ± 10 nm (see Fig. 5b). The microstructure of the ST + A material after ECAP shows the presence of elongated grains with fine fragmented precipitates distributed throughout the Al matrix (see Fig. 5c). The grain size at this condition is measured to be 250 ± 10 nm. The similar precipitate fragmentation during ECAP has been reported earlier in 7034 Al alloy [28, 29].

In recent times, Liu et al. [30] has shown that the dissolution rate for the deformable θ' precipitate phase (disordered, underage) in Al–Cu binary alloy system is far more than that of the brittle, un-deformable (ordered, overage) θ particles. The difference has been attributed to the accumulated strain energy as well as the formation of sub-boundary in the θ' phase during early cycles in ECAP. During later cycles, dissolution occurs through the sub-boundaries due to the preferential channel diffusion of Cu atoms. In contrast, the stable θ phase needs to be fragmented into smaller sizes since the critical radius for dissolution is much smaller for these particles to satisfy the interfacial energy criterion. In this study, the as-received starting material is under-aged and the precipitates are present as a result of previous processing. The precipitates in the ST + A starting material, on the other hand, are peak-aged and hence ordered and un-deformable. It is, therefore, possible for the precipitates present in the as-received starting material to dissolve during ECAP at a much faster rate than those present in ST + A starting material. The dissolution of coarse precipitates (~90 nm) in the as-received material after ECAP is also helped from their low volume fraction in the microstructure. The ST + A starting material exist in peak-aged condition and both the precipitate size and volume fraction are comparatively higher than the as-received material. Similar such dissolution behavior has been reported for precipitate phase for other class of aluminum alloys in [27, 28].

The hardness variation as a function of ECAP passes for the three materials is shown in Fig. 6. The ST + A material observed higher hardness because of the strengthening effect from grain refinement, precipitates, and dislocations.

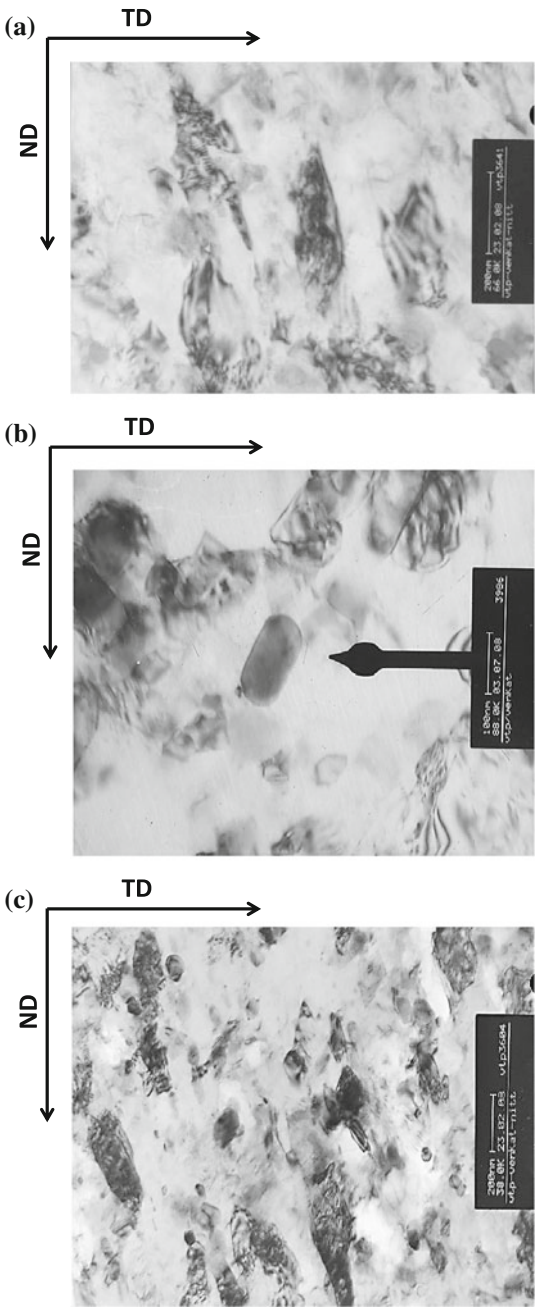

Fig. 5 Bright field TEM micrographs showing the microstructures after ECAP for **a** as-received condition, **b** after solution treatment, and **c** at solutionised + aged condition. *ND* normal direction, *TD* transverse direction, and *ED* extrusion direction which is normal to the plane of the micrograph

In the other two materials, the strengthening contribution from precipitates is absent. In the as-received material, it is anticipated that the fine precipitates got sheared and dissolved in the matrix during ECAP. In this case, the strengthening could be due to the grain refinement and by increased dislocation density (see Fig. 7). A similar behavior of dissolution of fine precipitates present in small

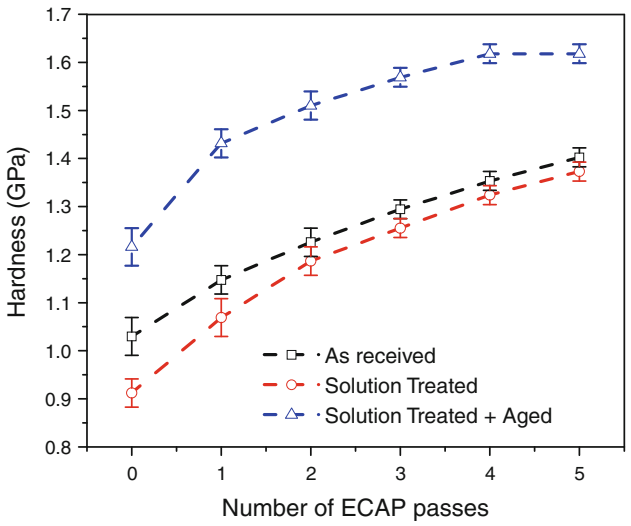

Fig. 6 Hardness variation as a function of number of ECAP passes for as-received, solutionised, and solutionised + aged materials

volume fraction was observed in severely deformed Al alloy [31].

X-ray diffraction line profile analysis (XRDLPA)

The crystallite size and dislocation density of the ECAP-processed materials was calculated from the X-ray diffraction data using the method originally proposed by Groma et al. [32, 33]. The calculations are based on the asymptotic behavior of the second and fourth order restricted moments of the diffraction data. The crystallite size and dislocation density obtained from XRDLPA for the three ECAP-processed materials are presented in Table 2. The table also includes the grain sizes measured from the TEM micrographs. The general observation is that the crystallite size calculated from XRDLPA is lower than the grain size measured by TEM. The difference between the results obtained by the two methods is due to the fact that the original grains in the starting materials are divided into sub-grains or dislocation cells during ECAP which are separated by low angle grain boundaries or dipolar dislocation domains separated by misorientation less than 1° or 2°. The crystallite size measured by XRDLPA represents the mean size of the coherent scattering domains. These domains are primarily the sub-grains or dislocation substructures that coherently scatter the incident X-ray. The grain size measurement from TEM micrographs, however, does not take into account the sub grains or for that matter the dislocation cells so that the grain size observed in TEM will be higher than the volume weighted mean crystallite size obtained from XRDLPA [34–36]. Nevertheless, the trend in the variation of crystallite size with the material conditions matches well to that of the grain size variation. The crystallite size is the highest in case of the as-received ECAP-processed material (240 ± 10 nm). For the ST material, the crystallite size as measured by XRDLPA is 230 ± 10 nm, which is lesser but quite close to the ECAP-processed material from the

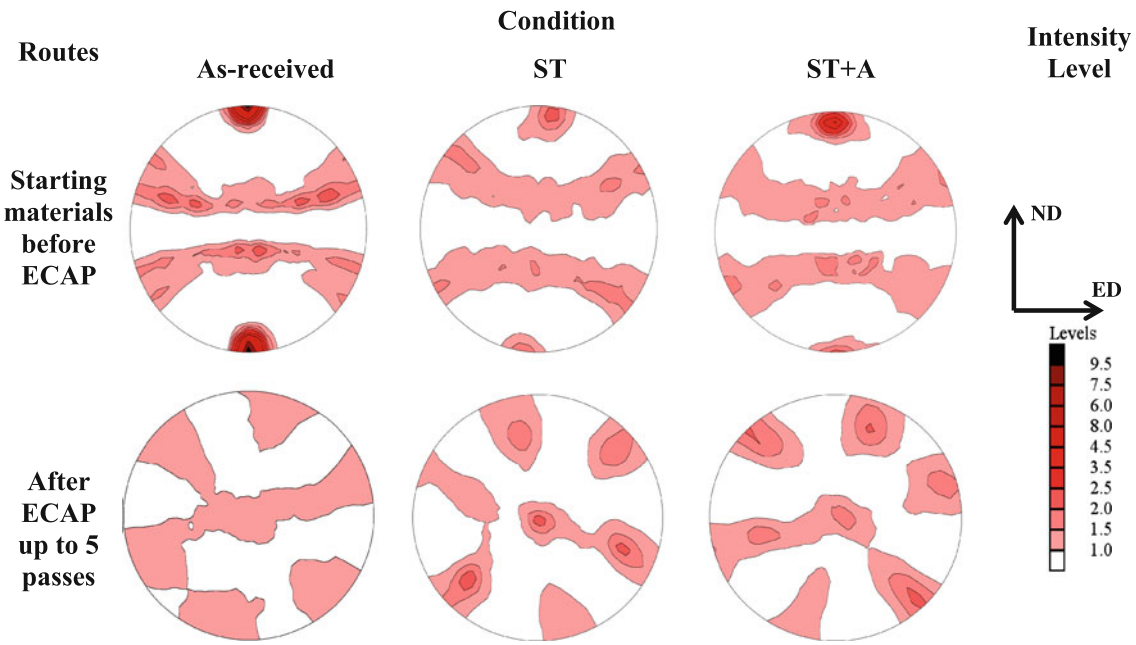

Fig. 7 Texture evolution in the starting as well as ECAP-processed materials shown in terms of (111) pole figure expressed in similar intensity level

Table 2 Grain size measured from TEM micrographs and crystallite size and dislocation density measured from XRDLPA analysis after ECAP processing up to five passes

Condition	Grain size from TEM (μm)	XRDLPA results	
		Crystallite size (nm)	Dislocation density × 10^{15} (m^{-1})
As-received	280 ± 10	240 ± 10	7.5 ± 0.5
ST	270 ± 10	230 ± 10	12 ± 0.5
ST + A	250 ± 10	150 ± 10	19 ± 0.5

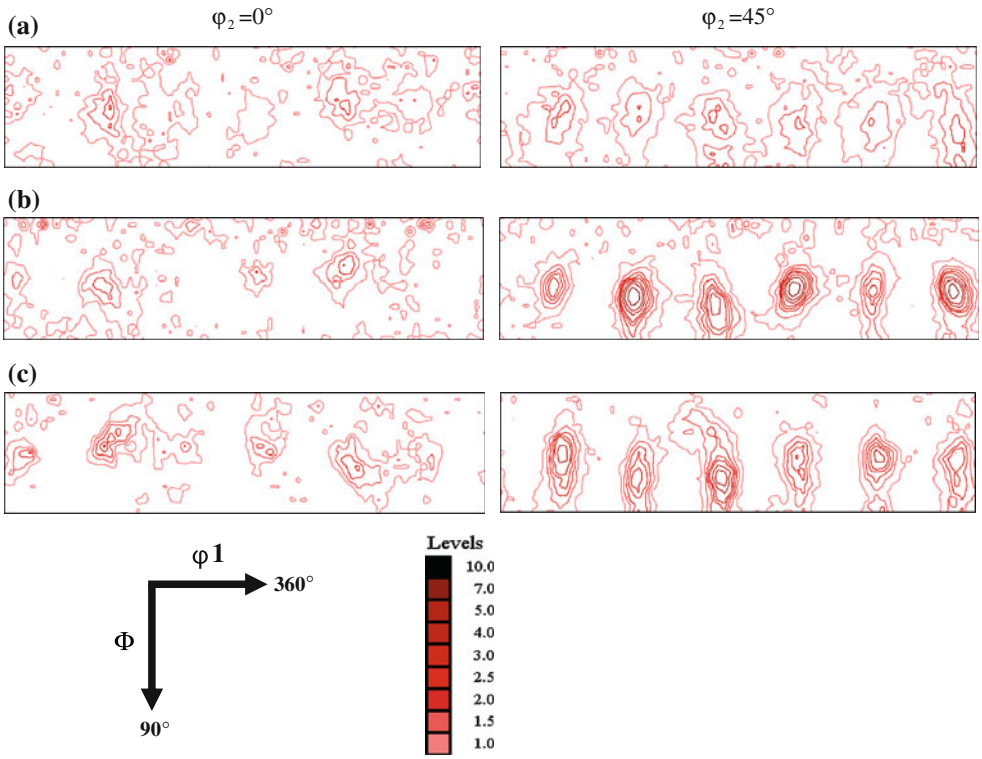

Fig. 8 $\varphi_2 = 0°$ and $\varphi_2 = 45°$ ODF sections after ECAP processing up to five passes on **a** as-received, **b** ST, and **c** ST + A materials. The intensity levels and the Φ and $\varphi 1$ directions are shown at the bottom

starting condition. For the ST + A material, a minimum crystallite size is obtained after ECAP (150 ± 10 nm).

The dislocation density (ρ) also indicates a systematic variation. The ST + A material shows the highest dislocation density of the three conditions ($\rho = 19 \pm 0.5 \times 10^{15}$ m^{-1}), whereas the ECAP-processed samples from the as-received and ST conditions contain dislocation densities of $7.5 \pm 0.5 \times 10^{15}$ and $12 \pm 0.5 \times 10^{15}$ m^{-1}, respectively. The large dislocation density after ECAP processing of solutionised plus aged material could be due to the dislocation pile up around the $CuAl_2$ precipitates. The dislocation density is less in as-received and solutionised materials because of the absence of precipitates in these materials.

Texture evolution

Figures 7 and 8 represent the texture evolution in the as-received, ST, and ST + A materials before and after ECAP processing up to five passes in terms of (111) pole figures and the relevant ($\varphi_1 = 0°$ and 45°) ODF sections. The pole figures and the ODF sections have been presented in the laboratory reference system projected onto the TD plane, which is initially parallel to the sample flow axis. The pole figures for all the materials are expressed with similar intensity (expressed as multiples of random unit) levels for the ease of comparison. The texture of the materials before ECAP was reasonably stronger than that of the corresponding materials after the ECAP processing, indicating a weakening of texture as a result of ECAP. Among the starting materials, texture was strongest in the as-received material and weakest in the ST material. After ECAP processing, however, the weakest texture forms in the as-received material wherein the other two materials show somewhat similar intensity of the ECAP texture.

In order to carry out a finer and quantitative analysis of texture, ODFs were plotted in the Euler's space. The Euler angles and Miller indices of the ideal orientations that

Table 3 The ideal orientations typically obtained for fcc metals as a result of ECAP processing [14]

Ideal components	Euler angles			Miller indices		
	φ_1	Φ	φ_2	ED	ND	TD
A_E	45	35.26	45	[2 $\bar{2}$0 9]	[20 $\bar{2}$ 9]	[112]
$\bar{A}_E$	225	35.26	45	[$\bar{2}$ 20 $\bar{9}$]	[$\bar{2}$0 2 9]	[112]
B_E	45	54.74	45	[27 $\bar{1}$00 73]	[100 $\bar{2}$7 $\bar{7}$3]	[111]
	165	54.74	45	[$\bar{1}$00 73 27]	[$\bar{2}$7 $\bar{7}$3 100]	[111]
$\bar{B}_E$	105	54.74	45	[$\bar{7}$3 $\bar{2}$7 100]	[73 $\bar{1}$00 27]	[111]
	225	54.74	45	[$\bar{2}$7 100 $\bar{7}$3]	[$\bar{1}$00 27 73]	[111]
A_{1E}	80.37	45	0	[6 $\bar{2}$5 25]	[25 3 $\bar{3}$]	[011]
	170.37	90	45	[$\bar{2}$5 25 6]	[$\bar{3}$ 3 25]	[110]
A_{2E}	9.74	45	0	[25 $\bar{3}$ 3]	[6 25 $\bar{2}$5]	[011]
	99.74	90	45	[$\bar{3}$ 3 25]	[25 $\bar{2}$5 6]	[110]
C_E	135	45	0	[$\bar{1}$00 $\bar{7}$1 71]	[100 $\bar{7}$1 71]	[011]
	45	90	45	[71 $\bar{7}$1 100]	[71 $\bar{7}$1 $\bar{1}$00]	[110]

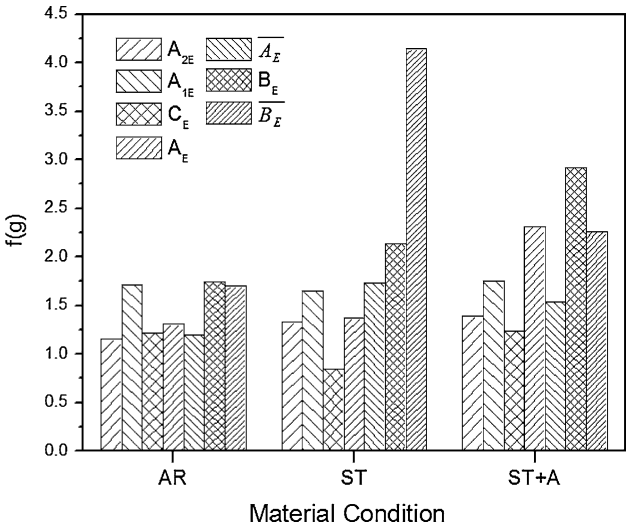

Fig. 10 Strength of various texture components in the as-received (AR), ST, and ST + A materials after ECAP processing up to five passes

typically form due to ECAP processing of fcc materials are listed in Table 3. Figure 8 shows $\varphi_2 = 0°$ and $\varphi_2 = 45°$ sections of the ODFs obtained for the ECAP-processed materials. The ODF sections were plotted up to 360° in the $\varphi_1$direction and 90° in the Φ direction. The locations of the ideal texture components that generally evolve during ECAP processing of fcc materials are presented in the key ODF in Fig. 9. Based on the key ODF, the ideal orientations are identified in the experimental ODFs. The absolute strength of the ideal texture components that evolved in the three materials after ECAP processing up to five passes are presented in Fig. 10. The texture components are, however, not located at the exact positions. Their deviations from the exact positions are listed in Table 4. The deviations are mostly observed along the φ_1 direction in the ODF which indicates a rotation of the texture components around the TD axis. The shifts are relatively low in all the conditions and the maximum deviation was observed for the A_{1E} component in ST condition. In can also be noticed that the component (110) [1$\bar{1}$1] which showed strong presence in all the starting materials (see Fig. 7), completely disappeared in all the ECAP-processed materials.

The ECAP-processed material from the as-received condition shows relatively lower shifts from the ideal orientation are relatively low in the $\varphi_2 = 0°$ and $\varphi_2 = 45°$ sections except for the $\bar{B}_E$ component. The $\varphi_2 = 0°$ section shows weak A_{2E} and C_E components in addition to a strong but wide spread A_{1E} component. In the $\varphi_2 = 45°$ section, relatively larger spread was observed around the ideal location of $A_E/\bar{A}_E$ and $B_E/\bar{B}_E$ components. In the $\varphi_2 = 45°$ section, continuous orientation distribution joining A_E, B_E, and C_E components in the ODF was observed which is generally denoted as B fiber in simple shear [17–20]. The absolute intensities of these components are quite weak and non-uniform spread is observed around the respective ideal positions. Similar weak connection between the components $\bar{B}_E$, A_{2E} and B_E, A_{1E} could be noticed.

For the ST material, the course of texture evolution after ECAP was different from the ECAP-processed material after the as-received condition. The strongest components in this case were $\bar{B}_E$ and $\bar{A}_E$. The weak C_E component, observed in the ODF of ECAP-processed material from the as-received condition does not appear in the ODF, when ECAP was carried out on the ST material. The other texture components e.g., A_{2E} and A_{1E} are, however, present in

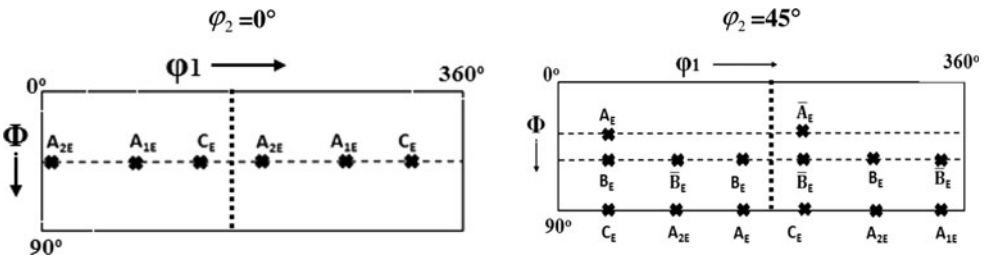

Fig. 9 Key ODF ($\varphi_2 = 0°$ and $\varphi_2 = 45°$) sections showing the locations of different ideal orientations in case of any ECAP-processed fcc material

Table 4 Absolute intensities of the ideal texture components measured for the three conditions after ECAP processing up to five passes. Also given are the deviations of these ideal components from their exact locations in the corresponding ODF sections (clockwise and anti-clockwise rotations are considered as positive and negative, respectively)

Condition	Intensity at maxima location (m.r.u)							Rotation w.r.t $\varphi 1$ from exact position (degree)						
	A_{2E}	A_{1E}	C_E	A_E	$\bar{A}_E$	B_E	$\bar{B}_E$	A_{2E}	A_{1E}	C_E	A_E	$\bar{A}_E$	B_E	$\bar{B}_E$
As-received	1.57	2.47	1.53	2.42	1.82	2.42	2.36	0	+2	+4	−4	+4	−4	+4
ST	1.89	3.27	1.16	3.85	5.36	4.88	9.48	0	+16	+4	0	+6	−4	+4
ST + A	2.47	3.15	1.92	6.86	3.32	6.86	3.23	−4	+6	0	−10	+4	−10	0

this case as well. Further, the B fiber shrinks to B_E component and another fiber between the components $\bar{B}_E$ and A_{2E} appears because of the strong intensity of $\bar{B}_E$ component. A similar fiber was also observed between the components B_E and A_{1E}. The contrasting feature in the texture of ECAP-processed material from the ST condition is that the components shown in the $\varphi_2 = 45°$ are strengthened and the spread is much reduced. Except for the A_{1E} component, the deviations from the respective ideal position were also quite low (see Table 4).

In the texture of ST + A material, the C_E component that was completely absent in the ECAP-processed material from the ST condition re-appears. A dissimilar intensity was observed for the pairs $A_E/\bar{A}_E$ and $B_E/\bar{B}_E$ for this material. The trend in the variation of the strength of individual components is different for this condition compared to that of the ST condition. In the ST condition, the components A_E and $\bar{A}_E$ are weak and strong, respectively. On the other hand, the trend is reversed for the texture of ECAP-processed material with ST + A as the starting condition. The components B_E and $\bar{B}_E$ follow a similar trend. The deviations of texture components from their respective ideal locations are much reduced in this case, except for the A_{1E} component. To summarize, the textures of ECAP-processed materials with ST and ST + A as the starting conditions are stronger than when the ECAP was performed on the as-received material. The major contribution is due to $B_E/\bar{B}_E$ components.

The important observation made in this study is that the B fiber (as seen in $\varphi_2 = 45°$ section) is weak in as-received condition, shrinks to only the B_E component in ST condition and finally spread along the A_E and B_E components in ST + A condition. The B fiber possibly forms during the initial ECAP passes and shrink to the A_E and B_E after five passes. Except for the as-received condition, a gradual strengthening in $A_E/\bar{A}_E$ and $B_E/\bar{B}_E$ components can be observed after ECAP. The major difference in texture between the ST and ST + A conditions was the weakening and strengthening of the A_{1E} and $\bar{B}_E$ components in the former material. The deviation in of the locations of the texture components is within 6° from the respective ideal positions for the materials ECAP processed from the as-received and the ST + A conditions. On the other hand, the deviation of A_{1E} component in ST condition extends up to 15° from its ideal position. The weakening of texture and deviation of components in ST + A condition could be a consequence of strain relaxation due to the precipitate fragmentation [18]. The fragmentation of precipitates might lead to strain gradients across the deformation zone leading to the weakening of texture components.

Conclusions

In this study, the effect of the starting microstructure on the texture evolution during ECAP of 2014 Al alloy through route A is examined. The important conclusions are summarized below:

1. ECAP processing of as-received, ST, and ST + A materials lead to significant grain refinement and precipitate fragmentation after deformation up to five passes. The amount of refinement is the lowest in ST + A material compared to that of the as-received and ST material.
2. Dislocation density considerably increased in case of ST + A material after ECAP due to the presence strain scattering from the coarse peak aged precipitates in the microstructure.
3. The strength of texture evolution strongly depends on the starting material condition. The absolute strength of ECAP texture varies in the order as-received material < ST + A material < ST material.
4. The texture strength variation is attributed to the strain scattering ability of the precipitates under imposed deformation conditions. The higher the strain scattering (as received and ST + A materials), the weaker the final texture evolution after ECAP.
5. The ECAP texture mainly consists of stronger $A_E/\bar{A}_E$ and $B_E/\bar{B}_E$ components and weaker C_E and A_{2E} components, rotated significantly by different amounts from their ideal positions.

Acknowledgements The authors are thankful to the NRCM, IISc, Bangalore and DRDO, New Delhi for technical and financial support. They express sincere gratitude to the Institute X-ray Facility at IISc for the required research facilities. The help rendered by Dr. Nilesh Gurao of IISc during the analysis of the texture results is also gratefully acknowledged.

References

1. Valiev RZ, Langdon TG (2006) Prog Mater Sci 51:881
2. Segal VM (1999) Mater Sci Eng A 271:322
3. Furukawa M, Horita Z, Nemoto M, Langdon TG (2001) J Mater Sci 36:2835. doi:10.1023/A:1017932417043
4. Lapovok R, McKenzie PWJ, Thomson PF, Semiatin SL (2007) J Mater Sci 42:1649. doi:10.1007/s10853-006-0967-x
5. El-Danaf EA, Soliman MS, Almajid AA, El-Rayes MM (2007) Mater Sci Eng A 458:226
6. Ferrasse S, Segal VM, Kalidindi SR, Alford F (2004) Mater Sci Eng A 368:28
7. Beyerlein IJ, Toth LS (2009) Prog Mater Sci 54:427
8. Abdulhakim AA, El-Danaf EA, Soliman MS (2009) J Mater Sci 44:5654. doi:10.1007/s10853-009-3796-x
9. Katsas S, Dashwood R, Todd G, Jackson M, Grimes R (2010) J Mater Sci 45:4188. doi:10.1007/s10853-010-4513-5
10. Suwas S, Massion RA, Toth LS, Fundenburger JJ, Eberhardt A, Skrotzki W (2006) Metall Mater Trans A 37:739
11. Skrotzki W, Scheerbaum N, Oertel CG, Brokmeier HG, Suwas S, Toth LS (2006) Mater Sci Forum 503:99
12. Suwas S, Toth LS, Fundenberger JJ, Eberhardt A (2005) Solid State Phenom 105:357
13. Skrotzki W, Scheerbaum N, Oertel CG, Brokmeier HG, Suwas S, Toth LS (2007) Acta Mater 55:2211
14. Suwas S, Massion RA, Toth LS, Fundenberger JJ, Beausir B (2009) Mater Sci Eng A 520:134
15. Massion RA, Suwas S, Toth LS (2005) Mater Sci Forum 495:839
16. Zhilyaev AP, Oh-ishi K, Raab GI, McNelley TR (2006) Mater Sci Eng A 441:245
17. Skrotzki W, Scheerbaum N, Oertel CG, Brokmeier HG, Suwas S, Tóth LS (2006) Mater Sci Forum 503–504:99
18. Chowdhury SG, Xu C, Langdon TG (2008) Mater Sci Eng A 473:219
19. Skrotzki W, Scheerbaum N, Oertel CG, Arruffat-Massion R, Suwas S, Toth LS (2007) Acta Mater 55:2013
20. Suwas S, Toth LS, Fundenberger JJ, Eberhardt A, Skrotzki W (2003) Scr Mater 49:1203
21. Kapoor R, Chakravartty JK (2007) Acta Mater 55:5408
22. Oh-ishi K, Zhilyaev AP, McNelley TR (2005) Mater Sci Eng A 410:183
23. Zhang K-F, Hong-hua Y (2009) Trans Non-ferrous Met Soc China 19:s307
24. Chang SY, Ahn BD, Hong SK, Kamado S, Kojima Y, Shin DH (2005) J Alloys Comp 386:197
25. Venkatachalam P, Ravisankar B, Kumaran S (2010) Int J Microstruct Mater Prop 5:88
26. Iwahashi Y, Wang J, Horita Z, Nemoto M, Langdon TG (1996) Scr Mater 35:143
27. Pawlik K (1986) Phys Stat Sol 134(b):477
28. Roven HJ, Manping L, Werenskiold JC (2008) Mater Sci Eng A 483:54
29. Xu C, Furukawa M, Horita Z, Langdon TG (2005) Acta Mater 53:749
30. Liu Z, Bai S, Zhou X, Gu Y (2011) Mater Sci Eng A 528:2217
31. Gutierrez-Urruti I, Munoz-Morris MA, Morris DG (2005) Mater Sci Eng A 394:399
32. Groma I (1998) Phys Rev B 57:7535
33. Borbely A, Groma I (2001) Appl Phys Lett 76:1772
34. May J, Dinkel M, Amberger D, Hoppel HW, Goken M (2007) Metall Mater Trans A 38:1941
35. Gubicza J, Ungar T (2007) Z Krist 222:567
36. Gubicza J, Balogh L, Hellmig RJ, Estrin Y, Ungar T (2005) Mater Sci Eng A 400:334